Amplitude saturation of MEMS resonators explained by autoparametric resonance

Document status and date:
Published: 01/01/2010

Document Version:
Publisher's PDF, also known as Version of Record (includes final page, issue and volume numbers)

Please check the document version of this publication:

• A submitted manuscript is the version of the article upon submission and before peer-review. There can be important differences between the submitted version and the official published version of record. People interested in the research are advised to contact the author for the final version of the publication, or visit the DOI to the publisher's website.
• The final author version and the galley proof are versions of the publication after peer review.
• The final published version features the final layout of the paper including the volume, issue and page numbers.

Link to publication

Download date: 23. Aug. 2022

Amplitude saturation of MEMS resonators explained by autoparametric resonance

Amplitude saturation of MEMS resonators explained by autoparametric resonance

C van der Avoort[1]**, R van der Hout**[2]**, J J M Bontemps**[1]**, P G Steeneken**[1]**, K Le Phan**[1]**, R H B Fey**[3]**, J Hulshof**[2] **and J T M van Beek**[1]

[1] NXP Research, Eindhoven, The Netherlands
[2] Department of Mathematics, VU University—Faculty of Sciences, De Boelelaan 1081a, 1081 HV Amsterdam, The Netherlands
[3] Department of Mechanical Engineering, Eindhoven University of Technology, PO Box 513, 5600 MB, Eindhoven, The Netherlands

E-mail: cas.van.der.avoort@nxp.com

Abstract

This paper describes a phenomenon that limits the power handling of MEMS resonators. It is observed that above a certain driving level, the resonance amplitude becomes independent of the driving level. In contrast to previous studies of power handling of MEMS resonators, it is found that this amplitude saturation cannot be explained by nonlinear terms in the spring constant or electrostatic force. Instead we show that the amplitude in our experiments is limited by nonlinear terms in the equation of motion which couple the in-plane length-extensional resonance mode to one or more out-of-plane (OOP) bending modes. We present experimental evidence for the autoparametric excitation of these OOP modes using a vibrometer. The measurements are compared to a model that can be used to predict a power-handling limit for MEMS resonators.

(Some figures in this article are in colour only in the electronic version)

1. Introduction

1.1. Power handling of MEMS resonators

MEMS resonators are being developed as timing devices for on-chip integration [1]. The mechanical resonance can be realized in many ways, of which bulk acoustical modes in silicon form only one family. These resonance modes can exhibit high-quality factors and high-resonance frequencies [2, 3]. Particularly, we consider devices fabricated in silicon-on-insulator (SOI) that vibrate in-plane (IP). The operation of such devices is characterized as the 'extensional mode' and the geometry is such that the device is thin compared to its length.

The mechanical resonator is to be incorporated in an oscillator loop. For a large signal-to-noise ratio one requires the mechanical vibration to be of an as large as possible amplitude. The actuation principle of the resonators being discussed is typically electrostatic. Electrostatic actuation induces *spring softening*, causing the resonance frequency to change to a lower value than the purely mechanical resonance frequency. Inclusion of more elaborate expressions for electrostatic actuation even allows us to predict the amplitude–frequency (A, f) behaviour for large signal actuation. This spring softening (or hardening for other types of resonators) has been labelled as a nonlinear limit for directly driven resonators [4]. In practice, however, this predicted maximum amplitude of vibration is not reached. Other effects distort the response. We propose that for extensional modes of vibration, *dynamic instability* poses a limit to the mechanical amplitude of vibration that can be reached. Dynamic instability can severely limit the power-handling capability of a MEMS resonator.

1.2. Autoparametric resonance

The dynamic instability of concern can be referred to as an autoparametrically excited unwanted resonance. Parametric

excitation, as opposed to direct excitation, is a method to bring an elementary mechanical system into resonance when the mechanical system can be described by the Mathieu equation, incorporating time-dependent variations of either stiffness or mass. This method of actuation has been demonstrated on MEMS cantilever structures [5]. Autoparametric excitation refers to an internal condition within an extended mechanical system. At least two equations of motion (hence two degrees of freedom) interact in such a way that the vibrational motion of one acts as a parametric driver for the other. Parametric and autoparametric resonance are well-studied subjects in mechanics. The excitation of bending modes by periodic compression of a slender structure was extensively studied for decades both in theory and experiments [6–8]. Recently, MEMS-related treatment of nonlinear dynamics was also published [9, 10]. Internal or autoparametric resonance conditions for multi-body mechanical systems or bodies with multiple eigenmodes were also subjected to experiments [11] and extensive modelling efforts [12, 13]. The occurrence of autoparametric resonance limits the power handling of MEMS resonators.

The organization of this paper is as follows. In section 2, we will discuss the extensional MEMS resonator under study. The actuation principle is detailed and experimental observations of saturated responses are presented. Section 3 focuses on the derivation of two coupled equations of motion comprising nonlinear coupling terms. In section 4, we derive closed-form expressions to predict the occurrence of saturation out of the equations of motion. Finally, we conclude our findings in section 5.

2. Measuring the power handling

2.1. Actuation of a MEMS resonator

Electrostatic actuation is a common way of driving a MEMS resonator. Here we discuss the effect this way of actuation has on the resonance frequency to be measured. Only small signal response is considered at this moment. After the fabrication process, a resonator results with a certain frontal area A facing an actuation electrode, separated by a narrow airgap g; see the top-view image of figure 1. When a voltage V is applied over this airgap, a resulting electrostatic force will be exerted on the face of the resonator, causing the tip to move to displacement x. This force is expressed as

$$F_{el} = \frac{\varepsilon_0 \varepsilon_r A V^2}{2(g-x)^2}, \tag{1}$$

and is a result of the capacitance between parallel plates in which the relative permittivity ε_r and the permittivity of vacuum ε_0 are used. Set $\varepsilon = \varepsilon_0 \varepsilon_r$. The voltage is a sum of a dc term and an ac part, $V = V_{AC} + V_{DC}$. The ac voltage swing is typically much lower than the dc level and $V_{AC} = v \cos \omega t$. For small amplitudes, we can approximate equation (1) using a Taylor series expansion around $x = 0$. This leads to

$$F_{el} = F(t) + k_{el} x, \quad \text{with}$$

$$F(t) = \frac{\varepsilon A v V_{DC} \cos \omega t}{g^2} \quad \text{and} \quad k_{el} = \frac{\varepsilon A V_{DC}^2}{g^3}. \tag{2}$$
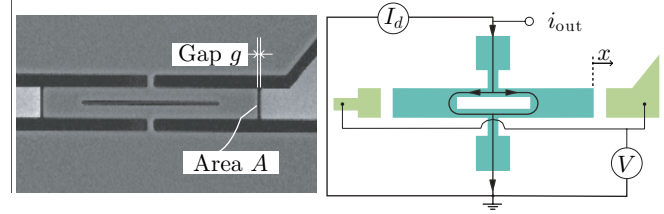

Figure 1. SEM micrograph and sketch of the MEMS resonator under study. A resistive output signal is measured by sending a current I_d through the resonator, which is electrostatically actuated by a voltage V, consisting of a biasing V_{dc} and a resonance-matched driving signal V_{ac}. The output is measured at the node labelled i_{out}. Area A is the *frontal* area, not visible in this top-view image, defined as material thickness times resonator width.

The angular resonance frequency ω is given by

$$\omega^2 = \frac{k_{eff} - k_{el}}{m_{eff}}, \tag{3}$$

where effective mass and stiffness are derived from the resonator geometry and material properties. The presented expressions show that we can control the resonance frequency by changing V_{DC}^2, whereas the driving force and hence the physical vibration amplitude will be controlled by the product $v V_{DC}$, where v is the amplitude of the ac voltage. We will employ this method of tuning frequency and controlling amplitude throughout the paper.

2.2. Experiments and observations

Our resonator is actuated and measured using an Agilent HP E5071C network analyser. The resonator and a connection scheme are depicted in figure 1. The extensional vibration, actuated by an ac voltage of amplitude v causes a change in the electrical resistance of the resonator, due to the piezo-resistive effect of doped silicon [14]. A dc current through the resonator will hence be modulated by the vibrating body. As a result, a transfer function from the applied ac voltage v to the sensed ac current i_{out} can be detected. By definition of port numbers, this transfer is defined as the transconductance

$$Y_{21} = i_{out}/v. \tag{4}$$

If the system is linear, then Y_{21} would be the same for all driving signal levels. However, figure 2 shows that for a driving voltage or power above a certain threshold value, the response is distorted. Increasing the applied driving power will lower the observed 'ceiling'. This observed *saturation* is the topic of this paper. Before we present our model to predict the occurrence of saturation, we extend our measurements to several biasing conditions.

Following equation (3) we can tune the frequency of the extensional vibration of the resonator by altering V_{DC}^2. As the actuation force $F(t)$ scales with V_{DC}, we will have to lower the driving power via the applied ac-voltage amplitude v accordingly for constant actuation force levels. For each shifted setting of the resonance frequency, we determine the maximum driving level that can be achieved and relate that to
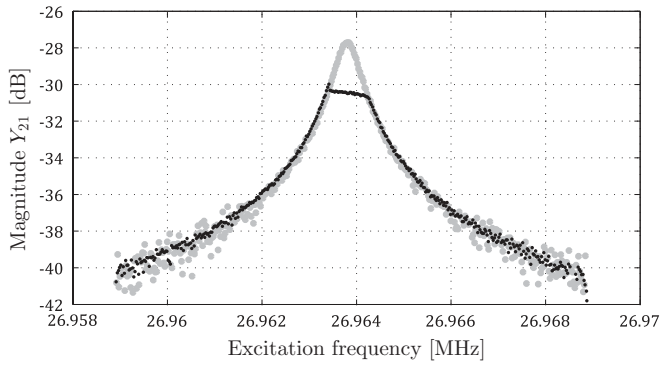
Figure 2. Two measurements of the same device. Grey discs: regular electrical response, plotted as an absolute value of transconductance (Y_{21}) versus excitation frequency. The output signal relates to the mechanical motion. Black dots: distorted electrical response, obtained by increasing the input power to the resonator. Since the measurement returns a transfer function, the increased input power only shows in the reduced noise.

the physical vibration amplitude. An elementary mass–spring system at resonance has a maximum vibration amplitude a of

$$a = F(t)\frac{Q}{k_{\text{eff}}}, \qquad (5)$$

where k_{eff} is the effective spring constant—relating the continuous body IP vibration to a single coordinate being the displacement of the tip—and Q is the quality factor, inversely scaling with the damping in the system. The electrostatic force $F(t)$ is known and renders the displacement amplitude at resonance to be

$$a = \frac{\varepsilon A}{g^2}\frac{Q}{k_{\text{eff}}}V_{\text{DC}}v, \quad \text{or} \quad a = \frac{\varepsilon\,Q\,8\,L\,V_{\text{DC}}\,v}{g^2\,E\,\pi^2}, \qquad (6)$$

where we have used that our resonator is a simple strip. For a strip of cross-sectional area A and length L we have, based on the mode shape of fundamental extensional vibration,

$$k_{\text{eff}} = \frac{EA\pi^2}{8L}. \qquad (7)$$

The Q factor is found from low-power frequency sweep measurements and E is Young's modulus of silicon. Figure 3 shows how at each setting of V_{DC}—or each setting of the electrostatic resonance frequency—the product $V_{\text{DC}}v$ can be increased until saturation occurs. It is observed that the physical vibration level for saturation to occur is far from constant. The minimum value for this particular resonator is about 0.1 V^2. Using equation (6) we can estimate the physical vibration amplitude of the resonator before saturation. Relevant geometric parameters are single-sided length $L = 68$ μm and airgap $g = 200$ nm. The measured Q factor is 49.000 in this case. This results for $V_{\text{DC}}v = 0.1$ V^2 in

$$a = \frac{\varepsilon Q 8L 0.1}{g^2 E\pi^2} = 0.46\,\text{nm}. \qquad (8)$$

For other biasing settings, see figure 3, yielding resonance near either 0 kHz or −40 kHz, the product $V_{\text{DC}}v$ and hence the physical vibration amplitude can be at least four times larger. We need an explanation for the fact that the maximum driving level shows a V-shape, but moreover we need to find why the
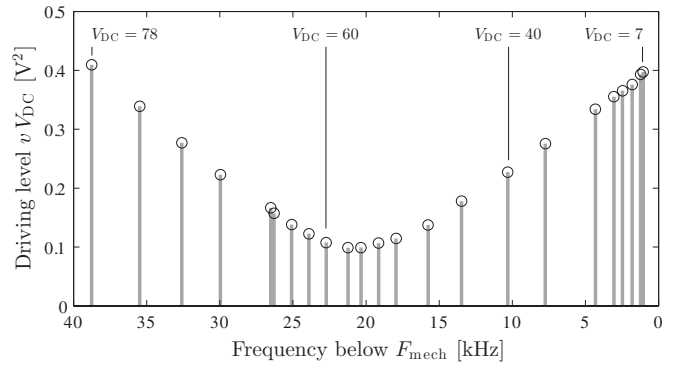

Figure 3. At each setting of V_{DC} the ac driving amplitude is increased until saturation occurs. The actuation force scales as $V_{\text{DC}}v$ where v is the amplitude of V_{AC}. The value of this product is recorded at each biasing setting.

resonator is limited to such a small amplitude of less than a nanometre.

Figure 4 was again measured on a single device, but of different geometry, resulting in a different in-plane resonance frequency. In this experiment again V_{DC}^2 was varied, but $v\,V_{\text{DC}}$ is now set to a number of levels, rather than increasing it until distortion occurs. We now superimpose all recorded functions $Y_{21}v$ that are scaled to represent amplitude a (nm). This resonator exhibits two minima of resonance amplitude. None of the limiting mechanisms found in the literature describe such behaviour.

2.3. Comparison of limiting mechanisms

In order to emphasize the need for a new model describing the observed saturation response, we list here other mechanisms that could limit the vibration amplitude of a MEMS resonator. The required vibration amplitudes for these effects to play a role will be analysed.

Firstly, the actuation airgap over which the electrostatic force acts is narrow. It measures 200 nm in our case. If the resonator acts as an impact oscillator [15], then the amplitude would be limited to this amount. Whether vibratory motion at such an amplitude is possible at all is arguable, as the point of electrostatic pull-in has been passed. The second possible cause for an effect on the maximum achievable amplitude is therefore pull-in. Certainly, approaching pull-in has a large effect on the vibration, not in the last part on the resonance frequency, as it will drop dramatically. Vibration after pull-in is not possible. The point of pull-in could be approached however, and vibration amplitudes of about 56% of the gap—112 nm in our case—would bring us into this regime. The pull-in limit to amplitude has been treated as a design guideline for limits to the power handling of a resonator [17]. The third possible limiting effect is referred to in the literature as the 'bifurcation limit' [4, 16]. Due to electrostatic actuation, the response of the driven resonator is susceptible to the (A, f)-effect, meaning that the resonance frequency is dependent on the vibration amplitude. As a result, a frequency response curve will be skewed rather than symmetrical. We will study the vibration amplitudes at which this effect plays a role more thoroughly.
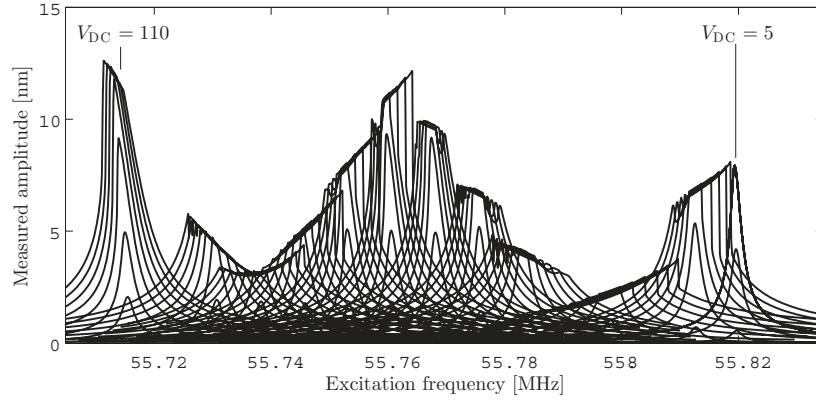
Figure 4. For many values of V_{DC} the response functions of a single device are recorded for multiple ac voltages v and translated to the physical vibration amplitude. As in figure 3 there is a frequency-dependent limit to the amplitude, but for this device there is more than one local minimum.

Appendix A explains the derivation of the electrostatic resonance frequency of a MEMS resonator including the (A, f)-effect. The angular IP resonance frequency Ω is given as (appendix A)

$$\Omega^2 = \frac{k_{eff}}{m_{eff}} - \frac{\varepsilon_0 A V_{DC}^2}{g^3 m_{eff}} - \left(\frac{a}{g}\right)^2 \frac{3}{2} \frac{\varepsilon_0 A V_{DC}^2}{g^3 m_{eff}}, \quad (9)$$

in which the first two terms were presented earlier—the mechanical frequency minus the shift due to V_{DC}^2—and the third term accounts for the amplitude-related contribution. Here, a is the vibration amplitude. The amount of amplitude-dependent behaviour is proportional to the amount of induced frequency shift. Here we already note that the (A, f)-effect is much larger for large biasing voltages and not easily encountered for the low values of V_{DC}. Moreover, this effect will only worsen, whereas our measurements in figure 3 show that after a minimum, the allowable amplitude rises again. Still, we want to perform a quantitative analysis and see if the 'bifurcation limit' predicts vibration amplitudes that correspond to the saturation we have observed.

The amount of skewing of the response curve can be related to the full width at half maximum (FWHM) which in turn directly relates to the definition of the quality factor Q. This width $\Delta\omega$ is expressed proportionally to the nominal resonance frequency so that

$$\frac{\Delta\omega}{\omega_0} = \frac{1}{Q}. \quad (10)$$

In turn, we also express the amount of skewing proportional to the nominal frequency. We label the third term in equation (9) now Θ so that we can express the proportional shift to be

$$\frac{\Theta}{\omega_0} = \frac{\Theta m_{eff}}{k_{eff}} = \left(\frac{a}{g}\right)^2 \frac{3}{2} \frac{\varepsilon_0 A V_{DC}^2}{g^3 k_{eff}}. \quad (11)$$

The above-mentioned bifurcation limit imposes that the skewing is so much, as compared to the width rendered by the Q-factor, that multi-valued solutions exist in the response curve. This is measured as hysteresis in up- and down-sweeps over frequency. We compare the amount of skew to the FWHM by taking the expressions from equations (10) and (11) to state

$$\Delta\omega = \Theta, \text{ so } \frac{1}{Q} = \left(\frac{a}{g}\right)^2 \frac{3}{2} \frac{\varepsilon_0 A V_{DC}^2}{g^3 k_{eff}}, \quad (12)$$

Table 1. Proposed power-handling limits found in literature for MEMS resonators compared to measured data. Evaluation of the bifurcation limit is rendered by third-order stiffness in the electrostatic actuation of the resonator. For various biasing voltages V_{DC}, the amplitude of vibration for bifurcation to occur is given, based on equation (13). Data are to be compared to the measured values presented in figure 3.

V_{DC} (V)	Bifurcation		Large Amplitude		Measured	
	$(vV_{DC})_{bif}$ (V^2)	a_{bif} (nm)	a_{obstr} (nm)	$a_{pull-in}$ $(nm)^a$	$(vV_{DC})_{meas}$ (V^2)	a_{meas} (nm)
7	47.86	217	200	112	0.40	1.82
40	8.38	38	200	112	0.23	1.04
60	5.59	25	200	112	0.11	0.50
78	4.30	20	200	112	0.41	1.86

[a] Pull-in occurs at 56% of the gap width, irrespective of the voltage over the gap.

which can be solved for amplitude a, yielding the bifurcation amplitude a_{bif}:

$$a_{bif}^2 = \frac{2g^5 k_{eff}}{3Q\varepsilon_0 A V_{DC}^2}. \quad (13)$$

Now we will determine whether our encountered amplitudes of saturation agree with a_{bif}. Equation (6) can be used to translate amplitudes a into driving levels $v V_{DC}$.

In table 1 we list the bifurcation limits found using equation (13). The required vibration amplitude in the case of our resonator is at least tens of nanometres for bifurcation to occur. The saturation effect that we have measured occurs already at an estimated vibration amplitude of less than 1 nm. There are orders of magnitude discrepancy between this amplitude and the derived bifurcation limit.

Concluding, we find that the presented explanations require too large vibration amplitudes in order to be able to explain our observed saturation level. Vibrations at the size of the gap width are hundreds of nanometres and the electrostatic actuation-related effects point to vibrations of tens of nanometres. Another effect lies at the basis of the observed saturation, and the saturation poses a serious limit to the power handling. In the following section, we propose
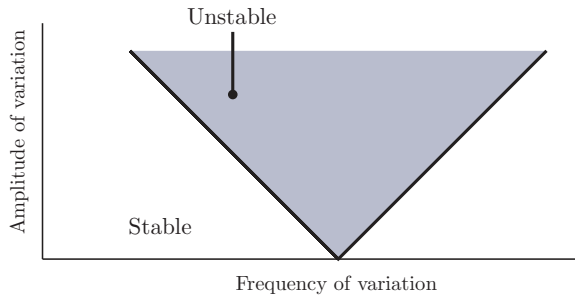
Figure 5. Sketch of one instability regime for a basic Mathieu equation. A not directly driven mass–spring system can start to oscillate at its fundamental resonance frequency when the amplitude and frequency of variation of either mass or spring constant lie within the sketched regime.

another mechanism and derive a model that can predict the occurrence of saturation. Moreover, the model also explains the biasing or frequency-dependent behaviour in figure 3.

3. Coupled equations of motion

We face the problem that our MEMS resonator shows a frequency-dependent limited amplitude and that in some cases this amplitude is very small. These two facts resemble the characteristics of the stability regimes of a Mathieu equation, an elementary equation of motion. It reads

$$\ddot{x} + \omega_0^2 \left[1 + \alpha \cos(\Omega t)\right] x = 0, \quad (14)$$

where ω_0 is the natural frequency, α is a small constant and Ω is the frequency of variation. In the absence of damping, the allowable amplitude α can even go down to zero, e.g. when $\Omega = 2\omega_0$, as sketched in figure 5. Practically, damping is always present, and the V-shape regime will be rounded off.

We propose that such a regime is to be attributed to a parasitic vibration. This can be a bending vibration or a torsional one, in any case *not* the intended length-extensional mode of vibration. A body such as a MEMS resonator has many different modes of vibration. If each of them can be caught in a Mathieu equation, then a multitude of instability regimes exists, as each single Mathieu equation in fact has multiple regimes of instability [18]. Moreover, there is the phenomenon of *combination resonance* to deal with [11, 13]. Basically, this means that when the frequency of variation (as for a single Mathieu equation) equals the sum or difference of the frequencies of two modes of vibration, then these two modes will start to oscillate in their fundamental frequencies.

This is in fact what is observed in the experiment presented in figure 4. Two regimes of instability exist, each of them related to a *pair* of parasitic modes of vibration. This knowledge was obtained using a Polytec laser vibrometer. At the moment when the extensional or IP response indicates saturation, we see a pair of out-of-plane (OOP) modes appearing.

Theoretically covering a complete instability landscape as in figure 4 is not intended at this moment. Nevertheless, we want to prove our hypothesis of parasitic vibrations causing

the saturation of the wanted vibration. To achieve a descriptive model for the observed frequency-dependent saturation, we have to take the following steps. First, we disregard combination resonance. Second, we focus on only one possible interaction of a parasitic mode with the intended mode. The dynamics of the resonator body are expressed in the equations of motion of two modal coordinates, associated with two mode shapes. To have coupling between these equations, we rely on an expression for mechanical strain that incorporates a correction term for large deformation.

3.1. Derivation of coupled equations

Figure 4 shows many measurements superimposed on one another. The measured IP extensional response truly saturates at a fixed level, for any V_{DC}. If more power is fed into the system, but the response is not increasing, it must mean that the additional energy is transferred into something else. In the following, we will show evidence that another mode of vibration consumes this additional energy. If this is a bending mode, then the IP electrical signal will not reveal this, as it is based on piezo-resistivity and requires a net strain in order to generate a signal. Bending about a neutral axis will, in first order, result in just as much positive as negative strain.

In what follows, we derive an interaction model for the driven mode of vibration and one bending mode. Generalization to include torsional modes and even combination resonance of multiple modes is possible, but not performed here. At the heart of the approach the chosen modes of vibration contribute to and interact via the potential energy of the vibratory system. We limit our model to just one parasitic bending mode that will be excited by the driven IP mode. After saturation, the bending mode is, in turn, at resonance, so the bending mode shape and the bending resonance frequency are not equal to that of the driven mode. For interaction to occur, we need the coupled equations of motion. To arrive at the coupled equations of motion, we choose the approach of Lagrange for our continuous system. This method relies on deriving expressions for the kinetic (T) and potential (V) energies in the total system. The equations of motion for every coordinate in vector **p**—in our case there are only two coordinates in this vector—then follow from the Euler–Lagrange equation [18]

$$\frac{\mathrm{d}}{\mathrm{d}t}\left(\frac{\partial T}{\partial \dot{\boldsymbol{p}}}\right) - \frac{\partial T}{\partial \mathbf{p}} + \frac{\partial V}{\partial \mathbf{p}} = \mathbf{F}, \quad \text{with} \quad \mathbf{p} = \begin{Bmatrix} p(t) \\ q(t) \end{Bmatrix}, \quad (15)$$

where the forces in **F** are the electrostatic force for the IP mode and zero for the OOP mode. The translation from continuous body motion to modal coordinates stems from the modal expansion theorem [18]. In the following sections, we want to focus on the coupling mechanism and therefore assume that the geometry of the bar under consideration is such that the fundamental IP (extensional) mode can be excited and that the first OOP bending mode is the only other possible mode of vibration.

We assume mode shapes along the x-axis and coordinates as the function of time t, see figure 6, according to

$$u(x, t) = p(t)\theta(x)$$

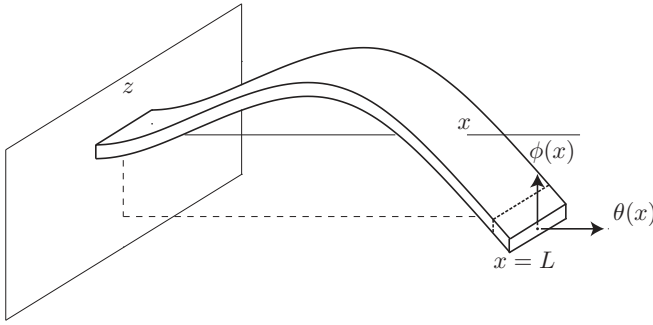$$w(x, t) = q(t)\phi(x), \quad (16)$$

Figure 6. Illustration of the coordinate system used and modal decomposition in one extensional mode of vibration $\theta(x)$ and one arbitrary bending mode of vibration $\phi(x)$. Note that the bending mode does not necessarily have to be the mode that is drawn here.
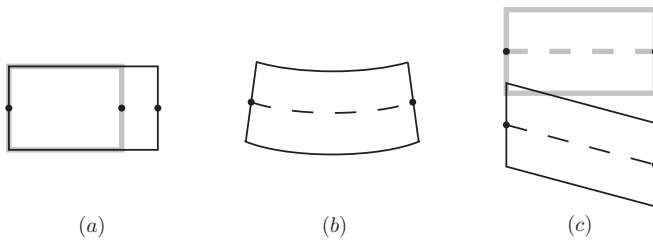

Figure 7. The potential energy of the coupled vibrations is based on strain in the x-direction only. It is constituted by (*a*) length extension, (*b*) curvature causing compression and extension and (*c*) length extension due to transverse displacement.

where the extensional displacement $u(x, t)$ is based on mode shape $\theta(x)$. Likewise for the bending mode the shape function $\phi(x)$ is a solution of the differential equation for the free vibration of a clamped cantilever. The vibration of a long slender bar is modelled one dimensionally. Both extension and bending can be described by a single displacement along the length of the beam, $u(x)$ and $w(x)$, albeit that two orthogonal directions of displacement x and z are considered. The kinetic energy contribution of every infinitesimal part of the beam is hence the sum of squared velocities in both displacement directions, whereas the potential energy for both vibrations is based on strain in only the x-direction. This strain, see figure 7, consists of three terms.

The kinetic energy is denoted as

$$T = \frac{1}{2}\rho A \int_0^L (\dot{u}^2 + \dot{w}^2)\, dx = \frac{1}{2}\rho A \int_0^L [\dot{p}^2\theta(x)^2 + \dot{q}^2\phi(x)^2]\, dx. \tag{17}$$

It should be noted that the integration over inner products of mode shapes mainly results in constants and for the motion we are interested in the time-dependent behaviour of the modal coordinates. Hence we write

$$T = \frac{1}{2}\rho A \dot{p}^2 \int \theta^2\, dx + \frac{1}{2}\rho A \dot{q}^2 \int \phi^2\, dx. \tag{18}$$

The potential energy is based on strain, which we define to be [19]

$$\epsilon = \frac{du}{dx} - z\frac{d^2w}{dx^2} + \frac{1}{2}\left(\frac{dw}{dx}\right)^2, \tag{19}$$

as illustrated in figure 7. The derivative of the extensional displacement du/dx is the definition of longitudinal strain. For bending the strain alters from compression to extension along the thickness coordinate z and is proportional to the inverse of the radius of curvature or the second derivative of the bending shape, d^2w/dx^2. Assumption of small displacement allows the neutral line to remain half the thickness. The last term in equation (19) corresponds to the approximated elongation of a beam piece when rotated over an angle dw/dx, while allowing the endpoints to move only vertically.

The definition in equation (19) will turn out to be the root of interaction between the two modes of vibration. The potential energy is expressed as

$$V = \frac{1}{2}Eb \int_{-h/2}^{h/2} \int_0^L \epsilon^2\, dx\, dz, \tag{20}$$

where the beam width b is used instead of area A, as integration over thickness has to take place. Inserting the modal expansion (16) and the definition of strain (19), we find that

$$V = \frac{1}{2}EA\left[p^2 \int \theta'^2\, dx + pq^2 \int \theta'\phi'^2\, dx + \frac{1}{4}q^4 \int \phi'^4\, dx \right]$$
$$+ \frac{1}{2}EI\left[q^2 \int \phi''^2\, dx \right], \tag{21}$$

in which area $A = bh$ and the second moment of area $I = \frac{1}{12}bh^3$ are based on the cross-sectional dimensions.

To construct the equations of motion the expressions for T and V can be inserted in the Lagrange equation, equation (15). The kinetic energy T does not depend on the position of any of the coordinates and $\partial T/\partial \mathbf{p}$ is zero. Furthermore, we see that

$$\frac{d}{dt}\left(\frac{\partial T}{\partial \dot{\mathbf{p}}}\right) = \rho A \begin{Bmatrix} \ddot{p}\int\theta^2\, dx \\ \ddot{q}\int\phi^2\, dx \end{Bmatrix}, \tag{22}$$

where the integrals are simplified and express the integration from 0 to L and θ and ϕ are the normalized displacement functions satisfying $\theta(L) = \phi(L) = 1$. For the potential energy we find

$$\frac{\partial V}{\partial \mathbf{p}} = \frac{1}{2}\begin{Bmatrix} EA\left(2p\int\theta'^2\, dx + q^2\int\theta'\phi'^2\, dx\right) \\ EA\left(2pq\int\theta'\phi'^2\, dx + q^3\int\phi'^4\, dx\right) + EI2q\int\phi''^2\, dx \end{Bmatrix}. \tag{23}$$

The mode shapes $\phi(x)$ and $\theta(x)$ lead to the scalar values for the inner products, rendering them as purely geometrical factors.

We combine equations (15), (22) and (23) and write the equations of motion as

$$\ddot{p} + \omega_1^2 p = -d_1 q^2 - \gamma_1 \dot{p} - G\cos(\Omega t)$$
$$\ddot{q} + \omega_2^2 q = -d_2 pq - \gamma_2 \dot{q} - d_3 q^3, \tag{24}$$

where the constants relate to the shape functions as

$$\omega_1^2 = \frac{E}{\rho}\frac{\int\theta'^2\, dx}{\int\theta^2\, dx}, \quad \omega_2^2 = \frac{EI}{\rho A}\frac{\int\phi''^2\, dx}{\int\phi^2\, dx}, \tag{25}$$

and

$$d_1 = \frac{E}{2\rho}\frac{\int\theta'\phi'^2\, dx}{\int\theta^2\, dx}, \quad d_2 = \frac{E}{\rho}\frac{\int\theta'\phi'^2\, dx}{\int\phi^2\, dx}, \quad d_3 = \frac{E}{2\rho}\frac{\int\phi'^4\, dx}{\int\phi^2\, dx}. \tag{26}$$

6

We have three different frequencies playing a role here, where ω_1 is the small-amplitude or linearized eigenfrequency of the IP mode, ω_2 is the eigenfrequency of the unwanted OOP mode and Ω is the forcing frequency. This system of equations can easily be integrated numerically in order to observe the time-dependent behaviour. Modal damping is added by γ_1 and γ_2, but exact estimation of damping values lies outside the scope of this paper.

3.2. A numerical example of the coupled equations of motion

Let us consider equation (24) more carefully. The equations show that the system is prone to autoparametric resonance. If p follows the harmonic motion, then it appears in (24*b*) as a time-variant spring constant. Hence, the equation of motion for bending in our system resembles a Mathieu equation.

The most pronounced instability regime for a Mathieu equation is found for a 2:1 ratio of the frequency of variation compared to the natural frequency. The natural frequency is, in our case, that of the bending mode, and the variation is, as explained, caused by the resonating extensional mode. To illustrate modal coupling most effectively, we set

$$\omega_1 = 2\omega_2, \quad \text{and} \quad \Omega = \omega_1. \tag{27}$$

The forcing frequency Ω hence drives the extensional mode exactly at resonance. If we apply damping ($\gamma_i \neq 0$) and set a certain driving force amplitude G, the system in equation (24) can numerically be integrated for 100 cycles of the IP mode, see figure 8. We see that from rest, the IP mode quickly gains amplitude. After about 50 cycles, one clearly sees that the OOP mode is arising. As it gains amplitude, the IP mode loses amplitude. Steady-state vibration is reached and both p and q remain at the fixed amplitude. The numerically produced result shows the co-existence of two states: quickly after the start we see $(|p|, |q|) = (3, 0)$ and after a number of oscillations this turns into $(|p|, |q|) = (2, 1)$. The *trivial* solution to the equations of motion in equation (24) should equal zero for the non-driven bending mode and a certain harmonic solution with an amplitude proportional to G for the driven IP mode. The *non-trivial* solution is, in this case, the steady state after 100 periods and relates to the coupling of modes. For this state, the amplitude of p is lower than its trivial counterpart and the amplitude of harmonic motion of q is larger than zero. In the following section, closed-form expressions to describe these states will be derived. It is interesting to observe the end amplitudes (as in figure 8) of both vibrations as a function of the driving amplitude G. Before pointing to a more sophisticated method to establish these steady-state amplitudes, figure 9 shows by ($\triangle$) and ($\triangledown$) the result of observing the ending amplitude of numerically integrating equation (24) with the parameters set as in figure 8 but for various values of the driving level G. The dashed lines in figure 9 are in agreement with the numerically found states but are actually drawn from the equations of motion in a closed form, to be derived in the following section.

The use of the parameter d_3 distinguishes figures 9(*a*) from (*b*). What we see in these figures could be labelled—considering the behaviour of the wanted IP mode—as 'pure saturation' (a) and 'perturbed growth' (b). Both situations can
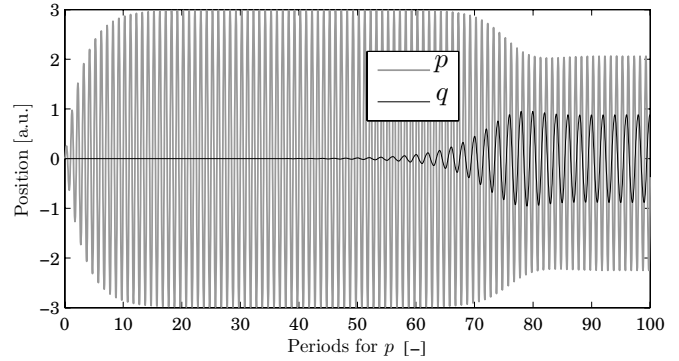

Figure 8. Integration of the system in equation (24), when $\omega_1 = 2\omega_2$, $\Omega = \omega_1 = 1$, $G = 0.3$ and $\gamma_1 = \gamma_2 = 0.1$, $d_1 = 0.25$, $d_2 = 0.05$, $d_3 = 0$.

be encountered in practice. As d_3 is the factor for third-order stiffness of the unwanted bending mode, it means that a non-zero d_3 causes a slight change of the frequency of the bending mode as its amplitude grows. Due to this amplitude-induced imperfectness of the 2:1 ratio, the driven IP mode can continue to rise in amplitude.

3.3. Closed-form expressions

Numerical integration of the equations of motion can be very time consuming. Typically, the steady state of a driven mass–spring system settles after a number of oscillations equal to the quality factor or the inverse of the damping constant. Moreover, such numerical evaluations will hardly provide quantitative insights into unexpected dynamical behaviour. Numerical continuation as a method for bifurcation analysis does a better job on insights, but still only select cases for set parameter values can be evaluated. We propose to use the method of *averaging* to derive closed-form expressions for the steady states of vibration from the given equations of motion. This method delivers us expressions for e.g. the maximum achievable IP amplitude, based on the basic parameters of the total system.

3.4. Application of the model to example cases

In appendix B we apply the method of averaging [20] to the coupled nonlinear equations of motion in equation (24). The method does not deliver $p(t)$ or $q(t)$, but rather the corresponding amplitude envelopes around the resulting vibrations. These envelopes have a magnitude and phase, $R_{1,2}$ and $\Phi_{1,2}$. A point in (R, Φ)-space corresponds to a steady harmonic vibration with a certain amplitude and phase-lag with respect to the driving force.

To illustrate the result of the averaging procedure, we present the expected amplitudes as a function of the driving force amplitude and of the driving frequency. The former can be considered a power sweep, whereas the latter a frequency sweep that is measured with a network analyser. One then performs a frequency sweep around the resonance frequency of the IP mode ω_1, so that a detuning parameter χ_1 can be introduced as

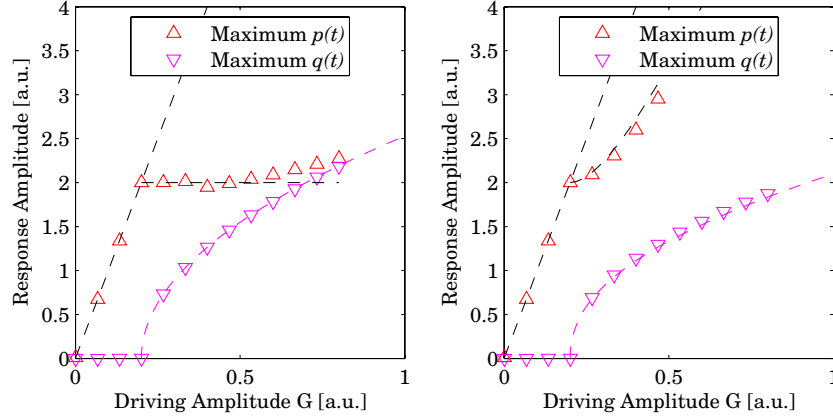$$\chi_1 = \omega_1^2 - \Omega^2. \tag{28}$$

Figure 9. Illustrations showing the saturation phenomenon. Numerical integration of equation (24) and taking steady-state amplitudes. When the excitation amplitude G is increased beyond the level where the OOP mode starts to oscillate, all energy 'fed' to the in-plane mode results in a higher amplitude of the OOP mode. The parameter d_3 then determines whether the steady-state amplitude of $p(t)$ can still grow. The dashed lines are drawn using the closed-form expressions derived in the main text. Parameter values: $\Omega = \omega_1 = 1$, $\omega_2 = 0.2$, $\gamma_1 = \gamma_2 = 0.1$, $d_1 = 0.25$, $d_2 = 0.05$. First plot: $d_3 = 0$, second plot: $d_3 = 0.05$.

The frequency matching condition for the parasitic mode as compared to the driven mode is not necessarily perfectly the 2:1 ratio, so that we introduce a second detuning parameter

$$\chi_2 = \left(\omega_2{}^2 - \frac{\Omega^2}{4} \right). \tag{29}$$

The frequencies that govern the system are now covered by the actuation frequency Ω and χ_i rather than ω_i. This allows our model to represent an actual measured frequency sweep response.

Example 1. The numerical case of the previous section.

As a first example of the closed-form expressions, we return to the results that we obtained by the numerical integration of the coupled equations of motion, as presented in figure 9. For this simulation we had excitation at resonance for the extensional mode and an exact 2:1 frequency ratio with the bending mode. The saturation level is then found—using the averaged system of equations—from equation (B.24) by setting $\chi_1 = 0$, $\chi_2 = 0$ and this results in

$$R_{1,\text{sat}}{}^2 = \frac{\gamma_2^2 \Omega^2}{d_2^2} + \frac{9 R_2^4 d_3^2}{4 d_2^2}. \tag{30}$$

When $R_2 = 0$, so when the bending mode did not take off yet, we see that R_1 saturates at a level determined by γ_2 and d_2. Apparently, the damping of the bending mode and the geometrical coupling strength of both modes control the saturation. More damping of the unwanted mode allows the wanted mode to achieve a larger amplitude. Additionally, equation (30) is a function of R_2. The evolution of R_2 versus the driving force amplitude G is found from the roots of equation (B.20). Again we set $\chi_1 = 0$, $\chi_2 = 0$. There are two branches, of which only one contains the stable solutions. The expression describing $R_2(G)$ is much more complicated than the inverse $G(R_2)$. We therefore write

$$g^2 = \frac{\gamma_1^2 \gamma_2^2 \Omega_4}{d_2^2} + \frac{d_1 \gamma_1 \gamma_2 \Omega^2}{d_2} R_2^2 + \left(\frac{d_1^2}{4} + \frac{9 d_3^2 \mu_1^2 \Omega}{4 d_2^2} \right) R_2^4, \tag{31}$$

so that we have constructed a fourth-order parabola. Function $R_2(G)$ will look like a square-root function translated from the origin. Figure 9 contains dashed lines representing equation (30) and the inverse of equation (31).

Example 2. A general frequency-dependent result

Purely as an example of what the closed-form expressions can describe, figure 10 shows both the responses of the extensional and the bending mode for certain arbitrary parameter settings. Such graphs, e.g. in [10], are usually only produced by numerical simulations based on continuation for the bifurcation analysis. In figure 10 we see stable R_1-solutions outside the trivial regular resonance response. Co-existence of solutions at a specific frequency does not mean that both turn up in a measurement. A likely sweep-up measurement of amplitude R_1 over this frequency span would follow trajectory A, then go down via B and up again to fall abruptly down to C at a frequency of about 1.4 and then continue the regular transfer function.

In detuning terms we can express the trivial, i.e. when $R_2 \equiv 0$, solution as

$$R_{1,\text{triv}} = \sqrt{\frac{g^2}{\gamma_1^2 \Omega^2 + \chi_1^2}}. \tag{32}$$

Equations (B.20) and (B.24) will also provide us with the non-trivial state (R_1, R_2) when $R_2 \neq 0$ when we substitute valid numbers for $(R_2)^2$. By having $(R_2)^2$ as variable, two roots of equation (B.20) can be found. These can subsequently be substituted in equation (B.24) although one will discover that only one solution for $(R_2)^2$ will correspond to a stable branch of solutions. For illustration, in figure 10 the two branches for $(R_2)^2$ are included in the plot. Based on system parameters and tuning the settings χ_1 and χ_2 the complete solution space can be rendered.

4. Experimental validation

We now return to the experimental data presented earlier in this paper. We are facing a saturation phenomenon that appears
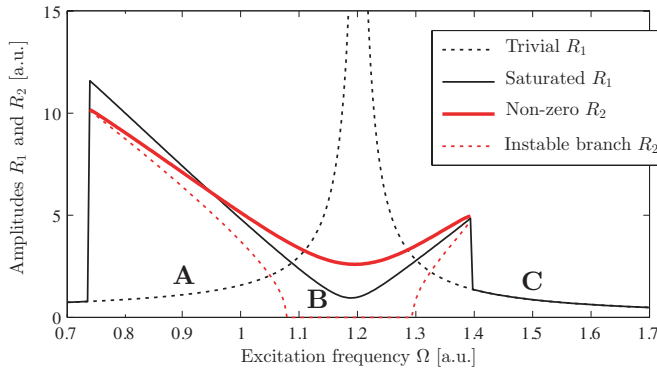
Figure 10. Illustration showing a possible response for appropriate model parameters. Apparently, a stable steady-state solution of the entire system exists, where the IP vibrations can be sustained *outside* the regular second-order transfer function. When sweeping the excitation frequency up, the response from the extensional vibration will likely stay on the branch of solutions labelled **A**, then follow **B** in the central region and to frequencies outside the regular transfer function, before dropping to this regular solution and continuing over **C**.

when we measure a frequency sweep at fixed power of our length-extensional resonator. The power at which saturation occurs is bias dependent. None of the available amplitude limiting mechanisms can predict the very early saturation that we encounter. We now project the model of coupled motion on the measured data.

4.1. *Experiment 1*: Fit to a single frequency response measurement

Figure 11 shows a single frequency sweep measurement of the IP or length-extensional resonance. By setting appropriate values for all parameters in the coupled system, the model prediction of the trivial and saturated IP response can be superimposed nicely on the data. The root cause for saturation lies in a non-zero amplitude R_2 of the unwanted mode.

4.2. *Experiment 2*: Fit to frequency-dependent series of measurements

Using the detuning coordinates $\chi_{1,2}$ and the system parameters, the governing equation of system states is derived. When $R_2 = 0$ at the onset of instability, equation (B.24) provides the maximum amplitude of the IP mode as

$$(R_1^\star)^2 = \frac{\gamma_2{}^2\Omega^2 + 4\chi_2{}^2}{d_2^2}. \tag{33}$$

This means that when $\chi_1 = 0$, i.e. when the resonator is driven as intended at resonance, the stable limit of the IP mode is determined by the damping of the *other* mode, the frequency matching χ_2 and a constant modal coupling factor d_2. The saturation level of the driven extensional mode $(R_1^\star)^2$ is minimal when $\chi_2 = 0$. At this point we have an exact 2:1 ratio between the driven mode and the unwanted bending mode.

Without further proof we state that an expression such as equation (33) for the frequency-dependent saturation level of our MEMS resonator can be applied to other interacting
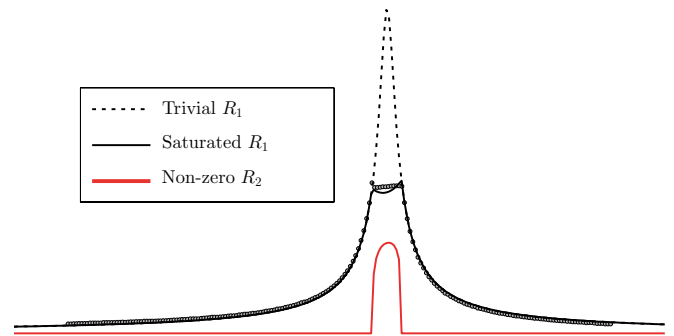

Figure 11. Using the derived expressions for steady-state amplitudes, the measured IP amplitude data (black dots) can be fit, including the saturation level (continuous line). The (unmeasured) corresponding OOP amplitudes are also plotted.
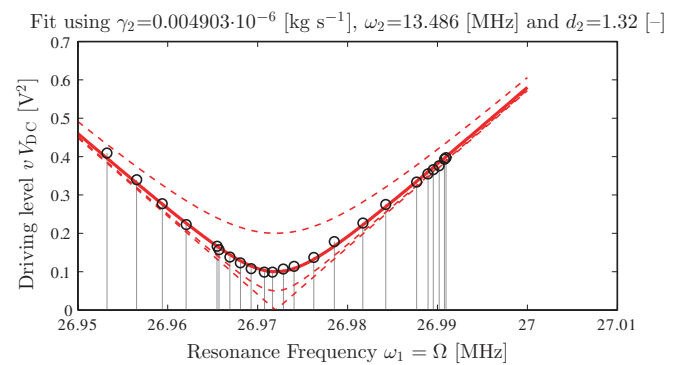

Figure 12. Data from the detuning experiment including our model fit. At various voltages and hence detuning settings χ_2, we observe the maximum amplitude $R_1^\star$ at the IP resonance ($\chi_1 = 0$). Fit parameters for equation (33) are indicated and correspond to the thick curve. Dashed lines indicate the maximum amplitudes when damping would be 0, 0.5 or 2 times the found value for γ_2.

modes—such as torsion—and even combination resonance. In figure 12 we have fitted equation (33) to the measured saturation levels presented in figure 3. Recall that $\chi_2 = (\omega_2^2 - \Omega^2/4)$ so that ω_2 is a fit parameter. The fitted line accurately follows the experimentally found maxima for changing amounts of detuning by V_{DC}^2. From figure 12 and equation (33) it is found that power handling is improved when $R_1^\star$ is large. This requires that $|\chi_2| \gg 0$ or $\gamma_2 \gg 0$, so that the unwanted mode should either be detuned far away or be damped sufficiently.

4.3. *Experiment 3*: Fit to excitation level-dependent measurements

Further proof of the versatility of our simplified model is presented in figure 13. Here we see a resonator with a 56 MHz IP resonance frequency being driven over the saturation limit. A torsional OOP vibration at 5.17 MHz starts to pick up energy. The expected modal interaction includes a third mode, so that combination resonance occurs. This third mode lies outside the bandwidth of our optical detection equipment. Only an interaction model for three modes of vibration could correctly describe this observation. However, when we compare our measurements of two modes to the two-mode model results in
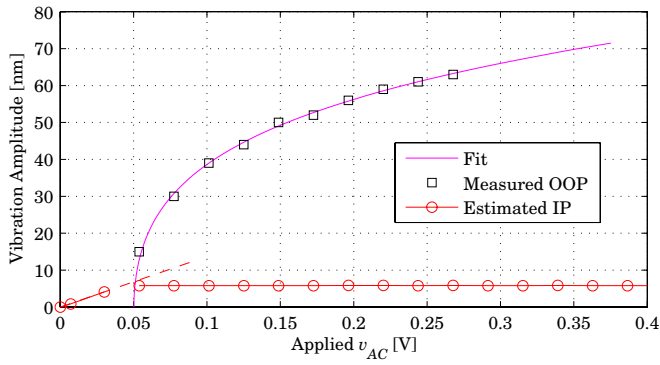
Figure 13. The IP amplitudes versus the driving voltage v derived from the measured electrical response and the OOP vibration amplitude measured optically using a Polytec vibrometer. The measurements are in fair accordance with the model results in figure 9.

figure 9, the difference—apart from the model parameters— lies only in the shape of the fit function of the OOP vibration amplitude versus the driving voltage. It is still an inversion of a fourth-order parabola. The predictive power of our model is satisfying, considering that it is a simplified model that does not govern all possible modes of interaction.

Summarizing, we have shown that our presented model for two-mode interaction, being one directly driven length-extensional mode and one bending mode, can describe the phenomena encountered for our MEMS resonator. Although various unwanted modes of vibration exist and even combination resonance can occur, we see that our simplified model covers the important characteristics of the limited power handling of a MEMS resonator. The obtained closed-form expressions provide a compact description of both the stable limit before interaction starts, equation (33), and the steady-state amplitudes of both modes while interacting.

Design guidelines for resonators that are less prone to early saturation are available with this equation. Non-zero damping factors favour stable response, in contrast to the goal

of maximizing resonator Q for which the air-pressure has to be as low as possible. Furthermore, frequency matching is important. As demonstrated, it is not only the frequency of the desired extensional mode of vibration that needs careful design.

5. Beating phenomenon

Apart from saturation, MEMS resonators can exhibit another phenomenon of nonlinear dynamics, referred to as *beating*. A frequency response measurement, such as depicted in figure 14, shows again a saturated response and additionally it shows that the saturated region is *enveloped* in magnitude, rather than having a fixed magnitude. This is a special case of saturation and our model can also be used to predict whether or not one will observe beating when the resonator is driven into saturation.

When a frequency sweep (figure 14) confirms that super-critical excitation is exerted, a time-series measurement of the IP displacement then shows a fast oscillating signal within a slowly evolving envelope. After a synchronous optical OOP measurement it was confirmed that the OOP motion (of lower angular frequency than the IP motion) is enveloped as well, see figure 15. Moreover, it can be observed that the two envelopes have equal periods and stay synchronous. Our two-coordinate model as presented is also capable of capturing this behaviour. Especially for hardly damped conditions, beating shows up clearly, see figure 16. Numerical time integration quickly becomes a nuisance for weakly damped systems, as settling times typically require an amount of simulated cycles that scales as the inverse of the damping factor. Again, closed-form expressions to determine whether beating will occur are desirable.

Figure 16 shows a settled 'steady-state' beating response produced by the numerical integration of equation (33). It should be noted that the shape of this envelope is very sensitive to changes in either of the parameters determining the coupled system. A very thorough study of the conditions for beating to occur has recently been carried out by Van der Avoort
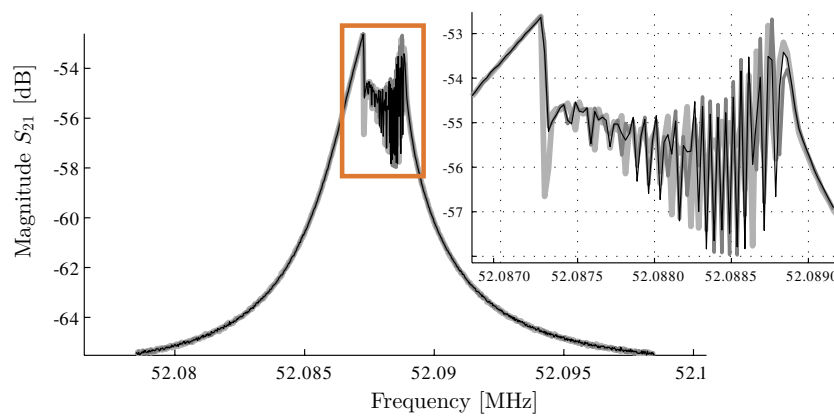

Figure 14. When the non-trivial response of the combined IP and OOP modes undergoes a Hopf bifurcation, the solution will not be a point but a trajectory through (R, Ψ)-space. Sampling this response at many frequency points results in an envelope rather than a point solution. Three series of data are taken for exactly equal conditions (indicated by different colours and line thicknesses). Only outside the beating region, where the trivial solution dictates the state of the system, do the three series coincide.
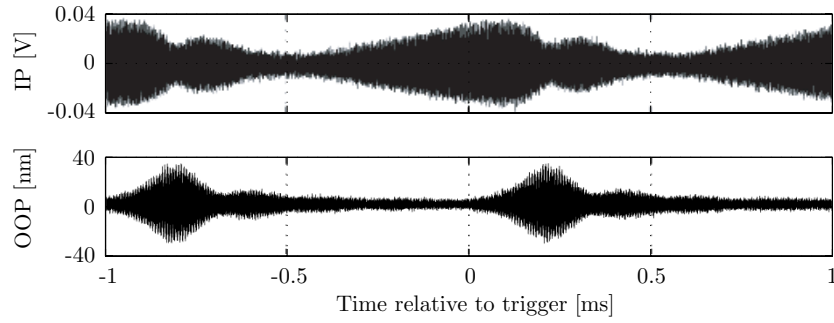
Figure 15. Example of observed beating in measured time-dependent data for a different resonator. The data for OOP motion have been taken using a Polytec vibrometer, while the IP motion was measured directly as an electrical signal. The IP signal corresponds to the electrically measured extensional vibration at about 19 MHz. The OOP signal is the optically measured displacement, which modulates at a different frequency. From the complementary amplitudes of the envelopes around the quickly modulating signals, it is clear that the two modes of vibration exchange energy.
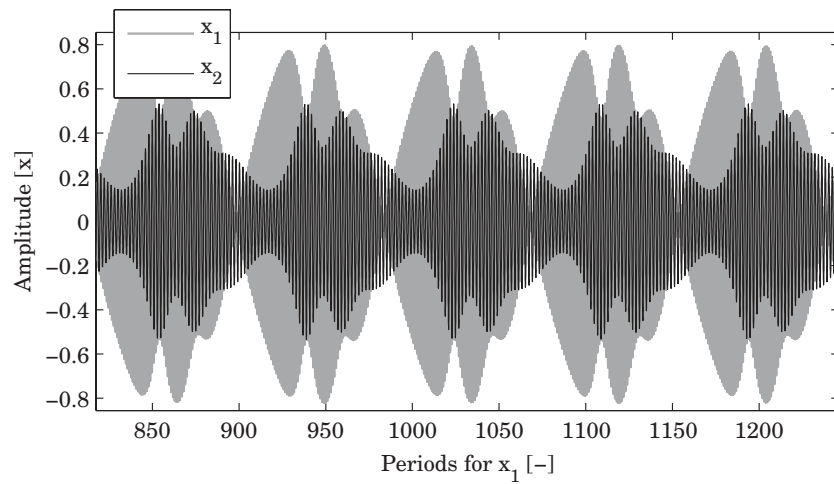

Figure 16. Illustration showing that in a long time-series numerical result obtained by our interacting equations of motion, a repeating pattern of vibrations arises in which energy is exchanged between the modes continuously.

et al [21]. Beating, or an unstable but bounded amplitude, is explained as the occurrence of a Hopf bifurcation in the (R, Φ)-solution space, considering the averaged equations of motion. The bifurcation alters the solution from a fixed point to a trajectory in solution space. In this space, a fixed point relates to a fixed amplitude of harmonic motion combined with a fixed phase-lag with respect to the external driving force. A trajectory in this space relates to time-dependent behaviour of these two coordinates of the solution. The trajectory is as fixed as a solution point, and as a result the beating pattern will exhibit a steady envelope. Estimates of the period of the beating envelope expressed in system parameters are beyond the scope of this paper.

The occurrence of beating in a system with multiple modes of resonance is not new, as already reported by Iwatsubo in 1974 [7, 8]. In their macroscopical experiments, instability regimes (in amplitude and frequency) of the directly driven mode are observed experimentally as well. Their observation that beating only occurs on one side of the regime, say only for negative detuning χ_2 in our terminology, is confirmed by the analysis by Van der Avoort *et al* [21]. The conditions for a Hopf bifurcation to occur can be expressed in terms of the parameters constituting our equations of motion,

equation (24). The analysis involves the stability analysis of the steady states and finding conditions for purely imaginary roots of the characteristic equation. The first condition is then

$$\left(\gamma_1^2 + 2\gamma_1\gamma_2\right)\Omega^2 + 12d_3\chi_2R_2^2 + 9d_3^2R_2^4 < 0, \qquad (34)$$

from which we already see that only one edge of the V-shaped instability curves can lead to beating. With d_3 being positive, as it is the integral over $\int(\phi')^4\,dx$, only $\chi_2 < 0$ fits the inequality. Only on one side of the exact 2:1 tuning can one encounter beating, whereas saturation into a stable combined solution is possible on both sides. A second condition for the imaginary roots is

$$d_1d_2R_2^2 > \gamma_1^2\Omega^2, \qquad (35)$$

so that a minimum amplitude for R_2^2 is required and large enough coupling constants d_1d_2, which in turn depend on the mode shapes of the interacting modes of vibration.

6. Conclusions

This paper describes the nature of saturation or limited power-handling capability observed for MEMS resonators. Autoparametric excitation of parasitic modes of vibration,

excited by the resonating intended mode of the vibration of the MEMS resonator, poses a limit to the amplitude of the vibration of the MEMS resonator. For one special case of modal interaction, closed-form expressions are derived that predict the saturation level of the IP vibration amplitude and show what factors influence the power-handling limit. As observed in experiments and predicted by the model, shifting the frequency of the MEMS resonator by bias voltage tuning will alter the saturation level. A second factor having an effect on the saturation level of the intended mode of vibration is the damping constant of the unwanted mode of vibration.

The saturation levels observed in measurements are generally lower than those predicted by the bifurcation limit found in the literature. Our model provides a description of a different mechanism for a limit. The saturation level is related to the physical vibration amplitude of the resonator, geometrical properties of the resonator and damping constants of both the wanted and the unwanted vibration, but at the same time it shows that saturation is *not* related to material nonlinearities or electrostatic spring softening.

Acknowledgments

Appendix A. Description of amplitude–frequency behaviour

In this section, we derive a closed-form expression for the frequency of a resonator under electrostatic actuation, including the (A, f)-behaviour. We will show that the resonance frequency is composed of a mechanically determined value, minus a shift that is controlled mainly by the squared biasing voltage V_{DC}^2 and finally a term in which the amplitude of vibration determines an additional negative contribution.

To drive a resonator to a stable amplitude, one has to overcome the damping force. Since this force scales with velocity, the most effective actuation force is also proportional to velocity. This means that the driving force is 90° out of phase compared to the harmonic vibration position function $x(t)$. We simply use an unknown gain factor K that relates the velocity of the resonator $v(t)$ to an ac-driving voltage V_{AC}. Our actual transduction mechanism is based on piezo-resistivity of the resonator and generates a signal that is proportional to *position*, but for the derivation of frequency we can assume a force proportional to *velocity*. The electrostatic driving force is now

$$F_{el} = \frac{\varepsilon A (V_{AC} + V_{DC})^2}{2(g - x(t))^2}, \quad \text{where } V_{AC}(t) = K v(t), \quad \text{(A.1)}$$

so that the driving voltage is directly coupled to the motion. It is proportional to velocity, since one wants to overcome damping which is, in turn, acting on the velocity as well. The electrostatic force F_{el} is position dependent, as the
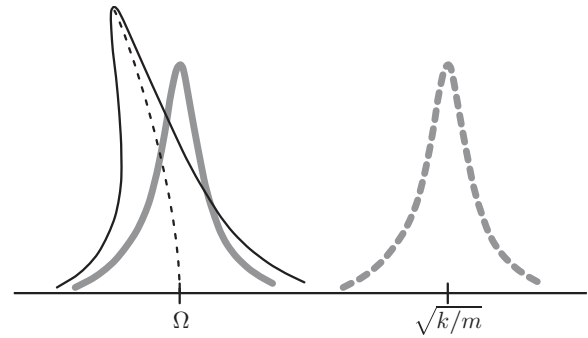

Figure A1. Sketch explaining the effect of electrostatic driving of a resonator on the to be measured frequency response. Geometry and material constitute a mechanical resonance frequency, $\sqrt{k/m}$. Due to a biasing voltage, the small-signal response is shifted towards a lower central frequency. Finally, for larger amplitudes—following the derivation in this appendix—a 'skew' of the response can be observed, which is a result of an amplitude-dependent resonance frequency.

displacement $x(t)$ reduces the airgap g. The standard form notation of the equation of motion of the driven resonator is then

$$\dot{v}(t) = \frac{F_{el} - kx(t) - \gamma \dot{x}(t)}{m}$$
$$\dot{x}(t) = v(t). \quad \text{(A.2)}$$

Next we use that the amplitude of $x(t)$ will be small compared to the airgap g, so that we can perform a Taylor series expansion to the third order of F_{el} around $x = 0$. The system of equations (A.2) is then transformed to polar coordinates by taking

$$x(t) = r(t) \cos(\Omega t + \theta(t))$$
$$v(t) = -\Omega r(t) \sin(\Omega t + \theta(t)), \quad \text{(A.3)}$$

of which the time derivatives are to be used as the left-hand sides of the equations of motion (A.2). The strategy for deriving the resonance frequency is now as follows. The coordinate transformation would render a linear oscillator in steady state motion into a single fixed point in (r, θ)-space. Nonlinearities cause other than purely sinusoidal motion, which in turn will be represented in (r, θ)-space as motion around a fixed point. To maintain this point fixed, the angular frequency Ω has to match the actual angular frequency of the modelled oscillator. A truly fixed point will have that $\dot{r}(t) = 0$ and $\dot{\theta}(t) = 0$, but with small jitter around a fixed point, this will never be the case. We need to *average* the transformed equations of motion, so that only fundamental dynamics prevail. Substituting equations (A.3) into equations (A.2) results after re-organization in a new system of equations of motion ($\dot{r}(t) = \cdots$ and $\dot{\theta}(t) = \cdots$) with very lengthy expressions involving combinations of time-dependent sin and cos factors. Since we are interested in the frequency of the harmonic motion, we can restrict ourselves to the fundamental harmonic. In order to do so, we average the transformed equations of motion over one period, according to

$$\dot{r}^A = \frac{\Omega}{2\pi} \int_0^{\frac{2\pi}{\Omega}} \dot{r}(t)\,\mathrm{d}t \text{ and } \dot{\theta}^A = \frac{\Omega}{2\pi} \int_0^{\frac{2\pi}{\Omega}} \dot{\theta}(t)\,\mathrm{d}t, \quad \text{(A.4)}$$

where the superscript A denotes the average quantities. Because the envelopes around the oscillatory motion, rendered by $r(t)$ and $\theta(t)$, will evolve slow as compared to the time-dependent sin and cos factors, we set the right-hand sides of the transformed equations of motion to have constant r and θ. Now the averaged equations of motion result. For the average radius or amplitude of vibration, this yields

$$\dot{r}^A = \frac{4g^2\varepsilon A K r^A V_{\mathrm{DC}} + 3\varepsilon A K (r^A)^3 V_{\mathrm{DC}} - 4g^4\gamma r^A}{8g^4 m}. \quad \text{(A.5)}$$

We need a steady-state (STST) vibration and hence require $\dot{r}^A = 0$. Equating equation (A.5) to zero leads to a solution for the gain factor K and reads

$$K_{\mathrm{STST}} = \frac{4g^4\gamma}{\varepsilon A V_{\mathrm{DC}}(4g^2 + 3(r^A)^2)}. \quad \text{(A.6)}$$

When we substitute this optimal K_{STST} for K, we can demand the solution to be fixed in the (r, θ)-plane by equating $\dot{\theta}^A = 0$. The resulting equation can be solved for Ω^2. This expression contains powers of r^A that are larger than the order of the expansion used for F_{el} in equation (A.2), and these higher order terms will be neglected. Inclusion up to the second order yields

$$\Omega^2 = \frac{k}{m} - \frac{\varepsilon A V_{\mathrm{DC}}^2}{g^3 m} - (r^A)^2$$
$$\times \left[\frac{3\varepsilon A V_{\mathrm{DC}}^2}{2g^5 m} + \frac{\gamma^2}{4g^2 m^2} - \frac{gk\gamma^2}{4\varepsilon A V_{\mathrm{DC}}^2 m^2} \right]. \quad \text{(A.7)}$$

In equation (A.7) we can see the influence of the damping constant γ on the resonance frequency. Since we are only interested in describing amplitude-dependent behaviour we neglect the γ-terms. This leads to the expression

$$\Omega^2 = \frac{k}{m} - \frac{\varepsilon A V_{\mathrm{DC}}^2}{g^3 m} - \frac{(r^A)^2}{g^2} \left[\frac{3}{2} \frac{\varepsilon A V_{\mathrm{DC}}^2}{g^3 m} \right], \quad \text{(A.8)}$$

which contains all aspects of electrostatic driving of a MEMS resonator and is visualized in figure A1. There is a mechanical frequency through k/m, which is shifted down by biasing with V_{DC}^2 and then is a function of the vibration amplitude (expressed now as compared to the gap). The latter term is proportional to the amplitude-*in*dependent shift rendered by the second term. Based on the assumption of a resonator in proper feedback—enough gain and no phase rotation apart from the 90 degrees between position and velocity—we have derived here a complete formulation of the electrostatic resonance frequency. This frequency will also be valid in an open-loop situation. The response curve in a frequency sweep will show shift and bending as well, with the presented r/g-dependent function as a central curve.

Appendix B. Coupled equations of motion subjected to averaging

The wanted and unwanted modes of the vibration of the resonator are described by the coupled equations of motion where the modal coordinates form the states of the dynamical system. Since cross-products between the states and higher powers of the states occur, a direct solution of the equations of motion is not possible. Several mathematical techniques exist to derive the closed-form expressions from these equations. Here we describe how *averaging* leads to expressions for the steady states of the system. There is one trivial steady state, where the directly driven mode has an amplitude proportional to the driving force amplitude and the other mode remains at zero. The non-trivial steady state describes the situation where the IP mode of vibration is saturated. The coupled equations are formulated with small-parameter notation as

$$x_1'' + \omega_1^2 x_1 = +\varepsilon\left(g\cos(\Omega t) - \delta_1 x_2^2 - \mu_1 x_1'\right),$$
$$x_2'' + \omega_2^2 x_2 = -\varepsilon\left(\delta_2 x_1 x_2 + \mu_2 x_2' + \delta_3 x_2^3\right), \quad \text{(B.1)}$$

where we have written

$$G = \varepsilon g, \quad d_i = \varepsilon\delta_i; \gamma_i = \varepsilon\mu_i. \quad \text{(B.2)}$$

Under the frequency matching condition of 2:1 with small detuning parameters we write

$$\omega_1^2 - \Omega^2 = \chi_1\varepsilon, \quad \omega_2^2 - \frac{\Omega^2}{4} = \chi_2\varepsilon, \quad \text{(B.3)}$$

so that we can write

$$x_1'' + \Omega^2 x_1 = \varepsilon\left(g\cos(\Omega t) - \chi_1 x_1 - \delta_1 x_2^2 - \mu_1 x_1'\right),$$
$$x_2'' + \frac{\Omega^2}{4} x_2 = -\varepsilon\left(\delta_2 x_1 x_2 + \chi_2 x_2 + \mu_2 x_2' + \delta_3 x_2^3\right). \quad \text{(B.4)}$$

Using the notation

$$y_1 = x_1, \quad y_2 = -\frac{x_1'}{\Omega}, \quad y_3 = x_2, \quad y_4 = -\frac{2x_2'}{\Omega}, \quad \text{(B.5)}$$

we write the system as

$$y' = Ay + \varepsilon f(y, t), \quad \text{(B.6)}$$

where

$$A = \begin{pmatrix} 0 & -\Omega & 0 & 0 \\ \Omega & 0 & 0 & 0 \\ 0 & 0 & 0 & -\Omega/2 \\ 0 & 0 & \Omega/2 & 0 \end{pmatrix}, \quad \text{(B.7)}$$

and $f(y, t)$ is in the vector form, following equation (B.4). With $u := \mathrm{e}^{-At} y$, we have the system

$$u_t = \varepsilon\,\mathrm{e}^{-At} f(\mathrm{e}^{At} u), \quad \text{(B.8)}$$

which is periodic in t, with period $T = 4\pi/\Omega$. In order to make the analysis tractable, we shall from now on study the averaged system. For details concerning the procedure of averaging, the reader is referred to [20]. Setting $\mathbf{u} := (u_1, v_1, u_2, v_2)^T$, we obtain

$$\begin{pmatrix} y_1 \\ y_2 \end{pmatrix} = \begin{pmatrix} u_1\cos(\Omega t) - v_1\sin(\Omega t) \\ u_1(\sin(\Omega t) + v_1\cos(\Omega t) \end{pmatrix};$$
$$\begin{pmatrix} y_3 \\ y_4 \end{pmatrix} = \begin{pmatrix} u_2\cos(\Omega t/2) - v_2\sin(\Omega t/) \\ u_2(\sin(\Omega t/2) + v_2\cos(\Omega t/2) \end{pmatrix}. \quad \text{(B.9)}$$

Note that a constant $\mathbf{u}$ represents a periodic orbit for the original system. Substitution leads to the expressions for $f(\mathrm{e}^{At}\mathbf{u})$ with

lengthy but straightforward terms. Averaging over period T leads to the equations of averaged u that read

$$\bar{u}_{1t} = \frac{-\varepsilon}{2\Omega}(\chi_1\bar{v}_1 + \mu_1\Omega\bar{u}_1 + \delta_1\bar{u}_2\bar{v}_2),$$

$$\bar{v}_{1t} = \frac{-\varepsilon}{2\Omega}\left(g - \chi_1\bar{u}_1 + \mu_1\Omega\bar{v}_1 - \delta_1\bar{u}_2^2 - \frac{\bar{v}_2^2}{2}\right),$$

$$\bar{u}_{2t} = -\frac{\varepsilon}{\Omega}\left(\chi_2\bar{v}_2 + \frac{\mu_2\Omega}{2}\bar{u}_2 + \frac{3\delta_3}{4}\left(\bar{v}_2^3 + \bar{u}_2^2\bar{v}_2\right)\right.$$
$$\left. - \frac{\delta_2(\bar{u}_1\bar{v}_2 - \bar{u}_2\bar{v}_1)}{2}\right),$$

$$\bar{v}_{2t} = \frac{\varepsilon}{\Omega}\left(\chi_2\bar{u}_2 - \frac{\mu_2\Omega}{2}\bar{v}_2 + \frac{3\delta_3}{4}\left(\bar{u}_2^3 + \bar{u}_2\bar{v}_2^2\right)\right.$$
$$\left. + \frac{\delta_2(\bar{u}_1\bar{u}_2 + \bar{v}_1\bar{v}_2)}{2}\right). \tag{B.10}$$

For determining the steady states of this system, it turns out to be advantageous to introduce the new unknown variables

$$z_1 := \bar{u}_1 + i\bar{v}_1; \; z_2 := \bar{u}_2 + i\bar{v}_2; \; z_3 := \bar{u}_2 - i\bar{v}_2; \; z_4 := \bar{u}_1 - i\bar{v}_1. \tag{B.11}$$

We rescale time in order to get rid of the factor $\varepsilon/2\Omega$. The equations (B.10) in this setting read

$$z_{1t} = -ig + (-\mu_1\Omega + i\chi_1)z_1 + \frac{\delta_1 iz_2^2}{2},$$

$$z_{2t} = (-\mu_2\Omega + 2i\chi_2)z_2 + \delta_2 iz_1z_3 + \frac{3\delta_3 iz_2^2 z_3}{2},$$

$$z_{3t} = -(\mu_2\Omega + 2i\chi_2)z_3 - \delta_2 iz_4z_2 - \frac{3\delta_3 iz_3^2 z_2}{2},$$

$$z_{4t} = ig - (\mu_1\Omega + i\chi_1)z_4 - \frac{\delta_1 iz_3^2}{2}. \tag{B.12}$$

By $Z_1, \ldots, Z_4$ we denote any steady state of this system. Then,

$$-ig + (-\mu_1\Omega + i\chi_1)Z_1 + \frac{\delta_1 iZ_2^2}{2} = 0, \tag{B.13}$$

$$(-\mu_2\Omega + 2i\chi_2)Z_2 + \delta_2 iZ_1Z_3 + \frac{3\delta_3 iZ_2^2 Z_3}{2} = 0, \tag{B.14}$$

$$-(\mu_2\Omega + 2i\chi_2)Z_3 - \delta_2 iZ_4Z_2 - \frac{3\delta_3 iZ_3^2 Z_2}{2} = 0, \tag{B.15}$$

$$ig - (\mu_1\Omega + i\chi_1)Z_4 - \frac{\delta_1 iZ_3^2}{2} = 0. \tag{B.16}$$

We shall write $R_1^2 := Z_1Z_4; \; R_2^2 = Z_2Z_3$. Obviously, there is a trivial steady state where $R_2^2 \equiv 0$, corresponding to IP oscillations of the resonator. It reads

$$\tilde{Z}_1 = g\frac{\chi_1 - i\mu_1\Omega}{\chi_1^2 + \mu_1^2\Omega^2}; \quad \tilde{Z}_4 = \overline{\tilde{Z}_1}. \tag{B.17}$$

We interpret the saturation phenomenon, as described in section 1, as the appearance of a new stable branch of solutions (namely: OOP oscillations), whereby the trivial steady state loses its stability. We shall now compute the nontrivial steady

states where $R_2 \neq 0$. To do that, we use (B.13) to express Z_1 in Z_2, and then plug the result into (B.14):

$$(-\mu_2\Omega + 2i\chi_2)Z_2 - \frac{\delta_2 g}{-\mu_1\Omega + i\chi_1}Z_3$$
$$+ \frac{\delta_1\delta_2 R_2^2 Z_2}{2(-\mu_1\Omega + i\chi_1)} + \frac{3}{2}\delta_3 iR_2^2 Z_2 = 0. \tag{B.18}$$

Similarly,

$$(-\mu_2\Omega - 2i\chi_2)Z_3 - \frac{\delta_2 g}{-\mu_1\Omega - i\chi_1}Z_2$$
$$+ \frac{\delta_1\delta_2 R_2^2 Z_3}{2(-\mu_1\Omega - i\chi_1)} - \frac{3}{2}\delta_3 iR_2^2 Z_3 = 0. \tag{B.19}$$

Considering R_2 fixed for the moment, these equations constitute a linear system in Z_2, Z_3; the existence of a nontrivial solution requires the determinant to vanish. That is,

$$\left(1 - \frac{6\chi_1\delta_3}{\delta_1\delta_2} + \frac{9\delta_3^2(\chi_1^2 + \mu_1^2\Omega^2)}{\delta_1^2\delta_2^2}\right)R_2^4$$
$$+ \left(\frac{4}{\delta_1\delta_2}(\mu_1\mu_2\Omega^2 - 2\chi_1\chi_2) + \frac{24\chi_2\delta_3(\chi_1^2 + \mu_1^2\Omega^2)}{\delta_1^2\delta_2^2}\right)R_2^2$$
$$+ \frac{4\mu_2^2\Omega^2 + 16\chi_2^2}{\delta_1^2\delta_2^2}(\chi_1^2 + \mu_1^2\Omega^2) - 4\frac{g^2}{\delta_1^2} = 0. \tag{B.20}$$

And reversely, if R_2 satisfies (B.20) then the system (B.18), (B.19) admits a solution with the property that $|Z_2Z_3| = R_2^2$. Writing

$$Z_2 = R_2 e^{i\Phi_2}, \; Z_3 = R_2 e^{-i\Phi_2}, \tag{B.21}$$

a simple computation yields that Φ_2 satisfies

$$\mu_1\mu_2\Omega^2 - 2\chi_1\chi_2 + \frac{(\delta_1\delta_2 - 3\delta_3\chi_1)R_2^2}{2} - i\left(\mu_2\Omega\chi_1 + 2\mu_1\Omega\chi_2\right.$$
$$\left. + \frac{3}{2}\delta_3\mu_1\Omega R_2^2\right) = \delta_2 g\, e^{-2i\Phi_2}. \tag{B.22}$$

It is now straightforward to compute Z_2 and Z_3. Note that Z_1 and Z_4 may be computed from (B.14) and (B.15):

$$-\delta_2 iZ_1 = (-\mu_2\Omega + 2i\chi_2)\frac{Z_2}{Z_3} + \frac{3\delta_3 iZ_2^2}{2},$$
$$\delta_2 iZ_4 = -(\mu_2\Omega + 2i\chi_2)\frac{Z_3}{Z_2} - \frac{3\delta_3 iZ_3^2}{2}. \tag{B.23}$$

To obtain R_1, we multiply these two equations and use that $Z_1Z_4 = R_1^2; \; Z_2Z_3 = R_2^2$:

$$\delta_2^2 R_1^2 = \mu_2^2\Omega^2 + 4\chi_2^2 + \frac{9}{4}\delta_3^2 R_2^4 + 6\delta_3\chi_2 R_2^2. \tag{B.24}$$

Substituting $R_2 = 0$ in (B.20) yields a value g^*, which is easily seen to be critical in the following sense: when $g < g^*$, the trivial steady state is stable, while for $g > g^*$ it is unstable. When $g = g^*$, $R_2 = 0$ and R_1 and R_2 satisfy (B.24), the nontrivial steady state branches off. The worst power handling occurs when $\chi_2 = 0$ so at an exact 2:1 condition. Then at the resonance of the IP mode ($\chi_1 = 0$) the maximum driving force amplitude is found from equation (B.20) to be

$$(g^\star)^2 = \frac{(\mu_2^2\Omega^2)(\mu_1^2\Omega^2)}{\delta_2^2}. \tag{B.25}$$

Increasing the damping of mode 1 or 2 or both will hence increase the power handling, but lowering the quality factor of the intended extensional mode of vibration is not wanted.

References

[1] Nguyen C T C 2007 MEMS technology for timing and frequency control *IEEE Trans. Ultrason. Ferroelectr. Freq. Control* **54** 251–70

[2] van Beek J T M, Verheijden G J A M, Koops G E J, Phan K L, van der Avoort C, van Wingerden J, Badaroglu D E and Bontemps J J M 2007 Scalable 1.1 GHz fundamental mode piezo-resistive silicon MEMS resonator *Proc. Int. Electron Devices Meeting (IEDM 2007)* pp 411–4

[3] van Beek J T M, Phan K L, Verheijden G J A, Koops G E J, van der Avoort C, van Wingerden J, Badaroglu D E, Bontemps J J M and Puers R 2008 A piezo-resistive resonant MEMS amplifier *Proc. Int. Electron Devices Meeting (IEDM 2008)* pp 667–70

[4] Kaajakari V, Mattila T, Oja A and Seppa H 2004 Nonlinear limits for single crystal silicon microresonators *J. Microelectromech. Syst.* **13** 715–24

[5] Turner K L, Miller S A, Hartwell P G, MacDonald N C, Strogatz S H and Adams S G 1998 Five parametric resonances in a microelectromechanical system *Nature* **396** 149–52

[6] Weidenhammer F 1951 Der eingespannte, achsial pulsierend belastete Stab als Stabilitätsproblem *Ing.-Arch.* **19** 162–91

[7] Iwatsubo T, Saigo M and Sugiyama Y 1973 Parametric instability of clamped-clamped and clamped-simply supported columns under periodic axial load *J. Sound Vib.* **30** 65–77

[8] Iwatsubo T, Sugiyama Y and Ogino S 1974 Simple and combination resonances of columns under periodic axial loads *J. Sound Vib.* **33** 211–21

[9] Kaajakari V and Lal A 2007 Micromachined ultrasonic motor based on parametric polycrystalline silicon plate excitation *Sensors Actuators* A **137** 120–8

[10] Vyas A, Peroulis D and Bajaj A K 2008 Dynamics of a nonlinear microresonator based on resonantly interacting flexural-torsional modes *Nonlinear Dyn.* **54** 31–52

[11] Cartmell M P and Roberts J W 1988 Simultaneous combination resonances in an autoparametrically resonant system *J. Sound Vib.* **123** 81–101

[12] Roberts J W and Cartmell M P 1984 Forced vibration of a beam system with autoparametric coupling effects *Strain* **20** (3) 123–31

[13] Nayfeh A H and Mook D T 1977 Parametric excitations of linear systems having many degrees of freedom *J. Acoust. Soc. Am.* **62** 375–81

[14] van Beek J T M, Steeneken P G and Giesbers B 2006 A 10 MHz piezoresistive MEMS resonator with high-*Q Proc. Int. Freq. Control System* pp 475–80

[15] Ya'akobovitz A, Krylov S and Shacham-Diamand Y 2008 Large angle SOI tilting actuator with integrated motion transformer and amplifier *Sensors Actuators* A **148** 422–36

[16] Abdolvand R and Ayazi F 2007 Enhanced power handling and quality factor in thin-film piezoelectric-on-substrate resonators *IEEE Ultrason. Symp.* pp 608–11

[17] Lin Y-W, Lee S, Sheng-Shian L, Xie Y, Ren Z and Nguyen C T-C 2004 Series-resonant VHF micromechanical resonator reference oscillators *IEEE J. Solid-State Circuits* **39** 2477–91

[18] Meirovitch L 1986 *Elements of Vibration Analysis* (New York: McGraw-Hill)

[19] Donnell L H 1976 *Beams, Plates and Shells* (New York: McGraw-Hill)

[20] Sanders J A, Verhulst F and Murdock J *Averaging Methods in Nonlinear Dynamical Systems* (Berlin: Springer) ISBN 978-0-387-48916-2

[21] van der Avoort C, van der Hout R and Hulshof J Parametric resonance and Hopf bifurcation analysis for a MEMS resonator *Physica* D submitted